

1 ***Neuropathy-related mutations alter the membrane binding properties of the human***
2 ***myelin protein P0 cytoplasmic tail***

3

4 Arne Raasakka¹, Salla Ruskamo^{2,3}, Robert Barker⁴, Oda C. Krokengen¹, Guro H. Vatne¹, Cecilie K.
5 Kristiansen¹, Erik I. Hallin¹, Maximilian W.A. Skoda⁵, Ulrich Bergmann^{2,3}, Hanna Wacklin-
6 Knecht⁶, Nykola C. Jones⁷, Søren Vrønning Hoffmann⁷ & Petri Kursula^{1,2,*}

7

8 ¹*Department of Biomedicine, University of Bergen, Bergen, Norway*

9 ²*Faculty of Biochemistry and Molecular Medicine, University of Oulu, Oulu, Finland*

10 ³*Biocenter Oulu, University of Oulu, Oulu, Finland*

11 ⁴*School of Physical Sciences, University of Kent, Kent, United Kingdom*

12 ⁵*ISIS Neutron and Muon Source, Science & Technology Facilities Council, Rutherford Appleton Laboratory, OX11
13 OQX Didcot, United Kingdom*

14 ⁶*Division of Physical Chemistry, Department of Chemistry, Lund University & European Spallation Source ERIC,
15 Lund, Sweden*

16 ⁷*ISA, Department of Physics and Astronomy, Aarhus University, Ny Munkegade 120, 8000 Aarhus C, Denmark*

17

18

19

20 *Corresponding author. E-mail: petri.kursula@uib.no

21

22

1 **Abstract**

2 Schwann cells myelinate selected axons in the peripheral nervous system (PNS) and contribute to fast
3 saltatory conduction *via* the formation of compact myelin, in which water is excluded from between tightly
4 adhered lipid bilayers. Peripheral neuropathies, such as Charcot-Marie-Tooth disease (CMT) and Dejerine-
5 Sottas syndrome (DSS), are incurable demyelinating conditions that result in pain, decrease in muscle mass,
6 and functional impairment. Many Schwann cell proteins, which are directly involved in the stability of
7 compact myelin or its development, are subject to mutations linked to these neuropathies. The most abundant
8 PNS myelin protein is protein zero (P0); point mutations in this transmembrane protein cause CMT subtype
9 1B and DSS. P0 tethers apposing lipid bilayers together through its extracellular immunoglobulin-like
10 domain. Additionally, P0 contains a cytoplasmic tail (P0ct), which is membrane-associated and contributes
11 to the physical properties of the lipid membrane. Six CMT- and DSS-associated missense mutations have
12 been reported in P0ct. We generated recombinant disease mutant variants of P0ct and characterized them
13 using biophysical methods. Compared to wild-type P0ct, some mutants have negligible differences in
14 function and folding, while others highlight functionally important amino acids within P0ct. For example, the
15 D224Y variant of P0ct induced tight membrane multilayer stacking. Our results show a putative molecular
16 basis for the hypermyelinating phenotype observed in patients with this particular mutation and provide
17 overall information on the effects of disease-linked mutations in a flexible, membrane-binding protein
18 segment.

19

20 **Keywords**

21 Myelin protein zero; membrane binding; peripheral neuropathy; CMT; DSS; disease mutation; gain of
22 function

23

24

1 Introduction

2 Fast saltatory nerve impulse conduction requires myelin, a structure composed of tightly stacked lipid
3 bilayers that wrap around selected axonal segments in the central and peripheral nervous systems (CNS and
4 PNS, respectively). The insulative nature of myelin enables efficient nerve impulse propagation, and the
5 destruction of myelin, demyelination, underlies a range of chronic diseases. In the PNS, peripheral
6 neuropathies affect Schwann cell compact myelin. These include Charcot-Marie-Tooth disease (CMT) and
7 its more severe, rapidly progressive form known as Dejerine-Sottas syndrome (DSS), which cause incurable
8 chronic disability (Hartline 2008; Stassart *et al.* 2018). CMT and DSS manifest through both dominant and
9 recessive inheritance, and they harbour a strong genetic component, typically caused by mutations in
10 proteins relevant for the formation and stability of PNS myelin, while axonal forms also exist.

11 Myelin protein zero (P0) is a type I transmembrane protein consisting of an extracellular immunoglobulin
12 (Ig)-like domain (Shapiro *et al.* 1996), a single transmembrane helix, and a 69-residue C-terminal
13 cytoplasmic tail (P0ct). P0ct is likely to be involved in the regulation of myelin membrane behaviour,
14 supporting the arrangement of the P0 Ig-like domains in the extracellular space upon the formation of the
15 myelin intraperiod line (Luo *et al.* 2007; Raasakka *et al.* 2019b; Wong and Filbin 1994). P0ct contains a
16 neuritogenic segment, which can be used to induce experimental autoimmune neuritis (EAN) in animal
17 models (de Sèze *et al.* 2016). *In vitro*, P0ct is disordered in aqueous solution, gaining secondary structure
18 upon binding to negatively charged phospholipids (Luo *et al.* 2007; Raasakka *et al.* 2019b). In its lipid-
19 bound state, P0ct affects the phase behaviour of lipids and promotes the fusion of lipid vesicles. High-degree
20 molecular order, most likely from stacked lipid bilayers, can be detected *via* X-ray diffraction of P0ct-bound
21 membranes (Raasakka *et al.* 2019b). This suggests that P0ct harbours a structural role in mature myelin.

22 Dozens of mutations have been identified in P0, most of which affect the Ig-like domain. These mutations
23 affect myelin morphology and integrity, leading to the development of peripheral neuropathies (Mandich *et*
24 *al.* 2009; Shy *et al.* 2004). Six known missense mutations are located within P0ct, of which four cause
25 dominant demyelinating CMT type 1B (CMT1B). These include T216ER (Su *et al.* 1993), D224Y (also
26 referred to as D195Y and D234Y) (Fabrizi *et al.* 2006; Miltenberger-Miltenyi *et al.* 2009; Schneider-Gold *et*
27 *al.* 2010), R227S (Shy *et al.* 2004), and the deletion of Lys236 (K236del) (Street *et al.* 2002). In addition,
28 K236E has been linked to dominant axonal CMT type 2I (CMT2I) (Choi *et al.* 2004), and A221T, which was
29 discovered as a co-mutation together with the deletion of Val42 in the Ig-like domain, was identified in a
30 patient with DSS (Planté-Bordeneuve *et al.* 2001). How these mutations relate to CMT/DSS etiology is not
31 known, although P0 mutations have been linked to the unfolded protein response (UPR) (Bai *et al.* 2013; Bai
32 *et al.* 2018; Wrabetz *et al.* 2006), indicating issues in either translation or folding that induce stress within the
33 endoplasmic reticulum (ER).

34 Considering the small size of P0ct and the nature of the disease mutations in it, many of which change its
35 electrostatic charge, impairment in the function of P0ct as a membrane binding/stabilizing segment is a

1 possible functional mechanism. We used methodologies established earlier for myelin basic protein (MBP)
2 (Raasakka *et al.* 2017) and wild-type P0ct (wt-P0ct) (Raasakka *et al.* 2019a; Raasakka *et al.* 2019b) to
3 characterize structure-function relationships of the CMT- and DSS-related P0ct variants. Our results suggest
4 that D224Y is a hypermyelinating gain-of-function mutation, which is in line with the clinically relevant
5 phenotype of abnormally thickened myelin sheaths (Fabrizi *et al.* 2006).

6

7

1 **Results**

2 We have earlier studied the binding of MBP and P0ct to model lipid membranes (Raasakka *et al.* 2017;
3 Raasakka *et al.* 2019a; Raasakka *et al.* 2019b), using a biophysical workflow that allows the determination of
4 binding affinity, gain in folding, alteration of lipid phase behaviour, quantification and visualization of
5 vesicle aggregation and fusion, and supported lipid bilayer (SLB) stacking. In the current study, we
6 examined whether and how CMT and DSS mutations within P0ct influence its structure and function. For
7 this purpose, we expressed and purified the wild-type protein and six mutant variants, each harbouring one of
8 the following amino acid changes: T216ER, A221T, D224Y, R227S, K236E, and K236del.

9

10 **Characterization of P0ct CMT mutants**

11 wt-P0ct and the six CMT variants were purified to homogeneity. Most mutants were straightforward to
12 purify, showing identical behaviour to wt-P0ct in size-exclusion chromatography (SEC) (Fig. 1b). D224Y,
13 on the other hand, had to be gel filtrated at a higher pH and salt concentration than the others, and while
14 yields were generally lower, minor amounts of degradation were present and the migration in SEC was
15 altered, albeit not in denaturing gel electrophoresis (SDS-PAGE) (Fig. 1b. Supplementary Fig. S1). In
16 dynamic light scattering (DLS), all variants displayed a similar hydrodynamic radius (R_h) and an absence of
17 aggregation (Fig. 1c, Supplementary Table 1). All of the variants showed high apparent molecular weight in
18 SDS-PAGE, which reflects the intrinsically disordered nature of P0ct (Raasakka *et al.* 2019b). The molecular
19 weight and the presence of the mutations were confirmed using mass spectrometry (Table 1). The total yields
20 of the purified mutant proteins were different from wt-P0ct (Supplementary Fig. S1, Table 1), most mutants
21 giving larger yields, with the exception of D224Y. It should be noted that all mutants were expressed as
22 maltose-binding protein fusions. Thus, mutations, which represent small changes in the overall sequence and
23 size of the fusion protein, can affect the expression and purification behaviour.

24 Small-angle X-ray scattering (SAXS) verified that for most variants, both the size and behaviour in solution
25 were nearly identical, with radius of gyration (R_g) and maximum dimension (D_{\max}) at 2.4 - 2.7 nm and 9.0 -
26 10.7 nm, respectively, and molecular masses matching monomeric protein based on I_0 values (Fig. 2,
27 Supplementary Table 2). D224Y presented a marginally larger D_{\max} (11.6 nm) compared to the other
28 variants, but all variants were flexible and extended in solution, as evident from the Kratky plot (Fig. 2d).

29

30 **The folding and lipid binding properties of P0ct CMT mutants**

31 To compare the conformation of the P0ct variants, we carried out a series of synchrotron radiation circular
32 dichroism (SRCD) spectroscopic experiments in the absence and presence of different lipid compositions,
33 detergents, and 2,2,2-trifluoroethanol (TFE), as previously described for wt-P0ct (Raasakka *et al.* 2019b).
34 P0ct is disordered in solution and gains a significant amount of secondary structure upon binding to small

1 unilamellar vesicles (SUV) with a net negative surface charge (Luo *et al.* 2007; Raasakka *et al.* 2019b). In
2 water, all mutants were disordered as expected, with D224Y having less secondary structure than the others
3 (Fig. 3). This is in agreement with the longer D_{\max} determined using SAXS. All mutants closely resembled
4 wt-P0ct in TFE and the detergents sodium dodecyl sulphate (SDS), *n*-dodecylphosphocholine (DPC),
5 lauryldimethylamine *N*-oxide (LDAO), and *n*-octyl glucoside (OG), while K236del was more α -helical than
6 the other variants in the presence of SDS (Fig. 3, Supplementary Fig. S2).

7 Addition of DMPC retained the proteins in a disordered state, with D224Y deviating slightly (Supplementary
8 Fig. S2). In the presence of net negatively charged SUVs composed of DMPC:DMPG ratios of 1:1, 4:1, and
9 9:1, the variants presented some folding differences (Fig. 3, Supplementary Fig. S2). Overall, most folding
10 was observed in 1:1 DMPC:DMPG, and the degree of folding decreased with decreasing fraction of DMPG,
11 *i.e.* negative charge. In DMPC:DMPG (1:1), a small shift to the right of the maximum at 188 nm was evident
12 for D224Y and K236del, indicating slightly increased folding, although the two minima at 208 and 222 nm,
13 typical for helical content, remained the same for all variants (Fig. 3d). In DMPC:DMPG (4:1), this effect
14 was only observed for D224Y (Fig. 3e). In DMPC:DMPG (9:1), the differences in signal magnitude were
15 large, reflecting different levels of turbidity (Supplementary Fig. S2). It can be assumed that the variants
16 showing high turbidity under this condition are membrane-bound, while the ones giving strong CD signal of
17 an unfolded protein do not bind to 9:1 DMPC:DMPG.

18 The affinity of P0ct variants towards immobilized DMPC:DMPG (1:1) SUVs was investigated using surface
19 plasmon resonance (SPR). All variants bound to lipids with similar kinetic parameters (Fig. 3f, Table 2),
20 including the A_1 value, which corresponds to the apparent K_d , of 0.35-0.4 μ M. This value is in the same range
21 with those obtained earlier for wt-P0ct, MBP, and P2 (Raasakka *et al.* 2017; Raasakka *et al.* 2019b;
22 Ruskamo *et al.* 2014; Wang *et al.* 2011). While the differences in K_d were minor, the behaviour of D224Y
23 was unique: the observed maximal response level was higher compared to the other variants. This suggests
24 that the D224Y variant can either accumulate onto immobilized vesicles in higher amounts, or it induces a
25 change on the surface that affects the measurement, such as the fusion, swelling, or aggregation of lipid
26 vesicles.

27

28 **Effect of CMT mutations on lipid membrane properties**

29 To determine the effect of the mutations on lipid structure, experiments probing changes in the
30 thermodynamic and structural properties of lipid membranes were carried out. As shown before (Raasakka *et*
31 *al.* 2019b), the presence of P0ct changes the melting behaviour of dimyristoyl lipid tails, inducing a
32 population that melts 0.9 °C below the major phase transition temperature of 23.8 °C. The presence of the
33 mutations altered this effect mildly (Fig. 4a), with T216ER and R227S behaving similarly to wt-P0ct. The
34 Lys236 mutations deviated from wt-P0ct, with a decreased temperature for the emerged population; K236E
35 and K236del showed lipid phase transition temperatures of 22.7 and 22.8 °C, respectively. A221T presented

1 slightly higher temperature for phase transition compared to wt-P0ct, with the major peak at 23.0 °C. Based
2 on the shape of the calorimetric landscape, D224Y was clearly different from the rest, as the new population
3 did not appear as a single, symmetric peak, but was rather formed of several overlapping peaks.

4 Similarly to MBP and P2 (Raasakka *et al.* 2017; Ruskamo *et al.* 2014), P0ct is capable of inducing
5 concentration-dependent solution turbidification, when mixed with lipid vesicles of net negative charge
6 (Raasakka *et al.* 2019b). The turbidity can arise from vesicle fusion and/or aggregation, and different
7 processes may be dominant in different samples with respect to the measured signal. To determine the effect
8 of P0ct CMT mutations on this function, turbidity experiments were carried out with the different variants.
9 T216ER and A221T produced turbidity levels similar to wt-P0ct (Fig. 4b, Supplementary Fig. S3a). At 1:100
10 P/L ratio, D224Y, R227S, K236E, and K236del all had decreased turbidity. At a P/L ratio of 1:50, however,
11 only D224Y had a significant inhibitory effect on turbidity. This result highlights that the D224Y mutant
12 protein may function differently from the other variants, when it binds to and aggregates vesicles.

13 To shed further light on the protein-induced changes in membrane structure, small-angle X-ray diffraction
14 (SAXD) experiments were performed on P0ct-membrane mixtures. In our earlier study, wt-P0ct mixed with
15 lipids produced two strong Bragg peaks, and the corresponding repeat distance evolved as a function of the
16 P/L ratio (Raasakka *et al.* 2019b). Here, we observed that in all cases, the repeat distance increased when
17 protein concentration in the sample decreased (Fig. 4c, Supplementary Fig. S3b). Each variant presented a
18 minimum repeat distance, which was reached at and above a P/L ratio of 1:100. The repeat distance for wt-
19 P0ct was ~7.5 nm, while D224Y produced a spacing of <7.0 nm. R224S, K236E, and K236del had looser
20 packing than wt-P0ct. K236E had a minimum repeat distance of ~8.0 nm at the highest protein
21 concentration.

22 To understand the effect of the mutations on the function of P0ct, and the origin of the high molecular order
23 reflected by X-ray diffraction, electron microscopy imaging was performed. Most mutants functioned in a
24 manner similar to wt-P0ct, producing large vesicular structures with a spread-out morphology (Fig. 5), with
25 occasional regions indicative of bilayer stacking. D224Y showed a clear difference to wt-P0ct, producing
26 strongly stacked myelin-like membranes in a manner resembling MBP (Raasakka *et al.* 2017). This gain of
27 function was reproducible over a wide range of P/L ratios (Supplementary Fig. S4) and a unique feature
28 among the six mutant P0ct variants. The results confirm that the Bragg peaks seen in SAXD, indeed,
29 originate from repeat distances in membrane multilayers, identically to two other PNS myelin peripheral
30 membrane proteins, MBP and P2 (Raasakka *et al.* 2017; Ruskamo *et al.* 2014; Sedzik *et al.* 1985). The
31 observed bilayer spacing for the D224Y mutant in EM was narrow and in general better defined than seen
32 for MBP (Raasakka *et al.* 2017), suggesting that P0ct forms a tight structure within and/or between the
33 membranes. Based on SAXD, the intermembrane spacing is ~3 nm, a value in close relation to the
34 dimensions of the major dense line (MDL) in myelin.

1 To gain an insight into the kinetic aspects of P0ct-induced lipid fusion/aggregation, stopped-flow kinetics
2 experiments were performed using SRCD (Fig. 6, Table 3) (Raasakka *et al.* 2019a). All variants followed a
3 similar kinetic pattern as wt-P0ct and could be best fitted to a two-phase exponential decay with two rate
4 constants (k_1 , fast and k_2 , slow). Rather minor differences were present: k_2 values were very similar in all
5 cases, and while D224Y presented 10% higher k_1 and k_1/k_2 compared to wt-P0ct and most other variants,
6 both K236E and K236del displayed k_1 and k_1/k_2 20% lower than for wt-P0ct, indicating slower kinetics (Fig.
7 6b). While all variants produced a similar end-level CD value around -100 mdeg, the starting level of
8 K236del was higher than for any other variant, and remained so until ~0.3 s, before settling on a similar level
9 to other variants. It is currently unclear whether this is due to an increased level of protein folding or less
10 scattered light from fused or aggregated vesicles.

11

12 **The membrane insertion mode of P0ct**

13 To understand the membrane insertion of P0ct, how it compares to MBP (Raasakka *et al.* 2017), and how it
14 might be related to disease mutations, we performed neutron reflectometry (NR) experiments (Fig. 7, Table
15 4). The insertion of P0ct to a DMPC:DMPG SLB was quite different to that of MBP. P0ct inserted
16 completely into the membrane, thickening it by 2 nm and increasing its roughness, most likely due to
17 increased bilayer mobility, as the hydration layer below the membrane became thicker (Fig. 7b,c). P0ct was
18 present in the acyl tail fraction of the membrane, as well as the outer headgroup fraction. The data could not
19 be fitted with only these parameters, but a very rough, narrow layer of protein had to be considered on top of
20 the membrane. Unfortunately, the roughness and high solvation fraction of this layer did not allow for
21 precise thickness determination: the layer was modelled to be between 5 – 15 Å thick within the fit to the
22 data. To investigate the effect of the D224Y mutation on P0ct membrane association, NR data were collected
23 for SLB-bound D224Y, which appeared identical to wt-P0ct (Supplementary Fig. S5).

24

25

1 **Discussion**

2 The formation of compact myelin and the major dense line requires an interplay of myelin molecules, many
3 of which have similar functional properties despite lack of sequence homology. Considering the MDL of
4 PNS compact myelin, the major protein components according to current knowledge are MBP, P2, P0ct, and
5 cytosolic loops of PMP-22. We characterized the potential functional anomalies of P0ct CMT mutants in
6 membrane binding using earlier established biophysical strategies (Raasakka *et al.* 2017; Raasakka *et al.*
7 2019a; Raasakka *et al.* 2019b).

8 The six mutations reported in P0ct are clustered within or near the neuritogenic segment. Most of them
9 reside in the vicinity of putatively phosphorylated Ser residues (Fig. 1a), which have been speculated to be
10 affected by P0ct mutations (Su *et al.* 1993; Xu *et al.* 2001). Many P0 mutations have been suggested to lead
11 to UPR activation (Bai *et al.* 2013; Bai *et al.* 2018; Wrabetz *et al.* 2006), indicating problems with translation
12 rate, folding, and/or membrane insertion. Given the fact that P0ct is known to interact with lipid membrane
13 surfaces (Luo *et al.* 2007; Raasakka *et al.* 2019b; Raasakka *et al.* 2019a), these mutations could also have
14 direct effects on the formation of mature compact myelin at the molecular level.

15 **Mechanism of P0ct binding to membranes**

16 In order to fully understand the effects of P0ct mutations on its structure and function, detailed knowledge
17 about P0ct binding to lipid membranes, and the effects thereof on multilayered membrane stacks, are
18 required. NR allowed us to gain a picture of P0ct in a lipid bilayer. P0ct inserts deep into a membrane, with
19 only a small fraction remaining solvent-exposed on the membrane surface. This is a clear difference to MBP,
20 which forms a brush-like protein phase on top of the membrane surface, while being partially embedded into
21 the bilayer (Raasakka *et al.* 2017). After undergoing charge neutralization and folding, P0ct seems to
22 collapse into a tight conformation and remain stable. The compact, deep conformation of P0ct suggests that
23 instead of directly embedding into two bilayers, which is the working model for *e.g.* MBP-induced stacking
24 (Raasakka *et al.* 2017; Vassall *et al.* 2015), P0ct may change the surface properties of the membrane in a
25 way that supports apposing bilayer surface adhesion. It could also regulate membrane curvature and the
26 twining of lipid bilayers around the axon.

27 At the level of full-length P0, P0ct is a direct extension of the transmembrane segment, and hence, anchored
28 permanently to a membrane surface at its beginning. Membrane stacking could involve the insertion of P0ct
29 across the MDL into an apposing membrane leaflet, which is only 3 nm away. Considering this scenario, P0
30 is basally expressed in Schwann cells even before myelination occurs (Lee *et al.* 1997). Moreover, P0 is
31 translated and inserted into the ER membrane and trafficked through the trans-Golgi network to the plasma
32 membrane after the Ig-like domain has been post-translationally modified (Eichberg 2002; Lemke and Axel
33 1985). If P0ct were to enter an apposing membrane during the formation of compact myelin, it would have to
34 remain in a disordered state until another membrane is present. On the other hand, if P0ct is embedded in the

1 membrane after translation, it might afterwards be able to dissociate and enter the apposing leaflet within
2 compact myelin. Considering the attractive phospholipid bilayer around the transmembrane helix, and the
3 fact that P0ct binds negatively charged lipids essentially irreversibly *in vitro*⁵, both mechanisms described
4 above are unlikely to exist. Thus, the role of P0ct in membrane adhesion is likely to be based on altered lipid
5 membrane properties, as opposed to MBP and P2, which directly interact with two membrane surfaces.
6 While P2 and MBP were observed to synergistically stack lipid bilayers *in vitro* (Suresh *et al.* 2010), mice
7 lacking both proteins formed apparently normal and functional myelin (Zenker *et al.* 2014). Hence, multiple
8 factors must participate in the correct formation of compact myelin; these include both lipid components of
9 the myelin membrane, different myelin proteins, as well as signalling molecules and inorganic ions. Hence,
10 further experiments in more complex sample environments are required to decipher the details of the
11 molecular interplay between these factors in PNS myelin MDL formation.

12 ***P0ct mutations and membrane interactions***

13 Compared to wt-P0ct, we observed only subtle differences for two mutants: T216ER and A221T. While
14 T216ER behaved very similarly to wt-P0ct, its role in CMT etiology could be of another origin than related
15 to protein-membrane binding. A221T, on the other hand, resides in the YAML-motif, which directs the
16 trafficking of P0 (Kidd *et al.* 2006) and might compromise the function of P0 even without inducing changes
17 in membrane binding, especially when combined with a second mutation in the extracellular domain, such as
18 the deletion of Val42 (Planté-Bordeneuve *et al.* 2001).

19 Functionally the most interesting mutant studied here is D224Y, which now has been described in at least 3
20 studies (Fabrizi *et al.* 2006; Miltenberger-Miltenyi *et al.* 2009; Schneider-Gold *et al.* 2010). It is a gain-of-
21 function mutant, inducing ordered lipid bilayer stacks *in vitro*, which are more tightly packed than those
22 formed by wt-P0ct or the other variants. The results correlate well the hypermyelinating disease phenotype
23 (Fabrizi *et al.* 2006). Neutron reflectometry produced a nearly identical result for D224Y compared to wt-
24 P0ct, which together with the SRCD experiments indicates that the conformation of wt-P0ct and D224Y is
25 similar in the membrane. The change of an acidic to an aromatic residue near the lipid bilayer surface most
26 likely enables a specific interaction between surfaces that results in the observed gain of function.

27 P0 is the most abundant protein in PNS myelin (Greenfield *et al.* 1973; Patzig *et al.* 2011), contributing
28 primarily to the formation of the intraperiod line (Filbin *et al.* 1990), and molecular mechanisms of D224Y-
29 induced tight stacking could be two-fold. Firstly, with its short repeat distance – 1-2 nm smaller compared to
30 MBP and P2 based on SAXD (Raasakka *et al.* 2019b; Ruskamo *et al.* 2014; Sedzik *et al.* 1985) – and active
31 membrane binding, as evident from SPR, the mutant might cause size exclusion of P2 and other factors out
32 of the cytoplasmic stack, leading to defective compact myelin maintenance. In PNS compact myelin, P2 is
33 even more abundant in the cytoplasmic compartment than MBP, can form membrane stacks, and harbours a
34 maintenance role in myelin homeostasis as a lipid carrier (Ruskamo *et al.* 2014; Zenker *et al.* 2014).
35 Secondly, the tendency of D224Y to form such ordered, tight systems might affect the Ig-like domains on the

1 extracellular side. In the hypermyelinating phenotype of D224Y patients, membrane stacking seems
2 condensed and regular, without abnormally loosened myelin (Fabrizi *et al.* 2006). SPR indicates that more
3 D224Y can accumulate on membranes, and full-length P0 D224Y could accumulate and tighten up within
4 the membrane, causing also the intraperiod line to become more crowded and/or structured. The original
5 discovery of the D224Y mutation (Fabrizi *et al.* 2006) suggested that it has a gene dosage effect, since
6 heterozygous carriers presented little to no symptoms. Hence, the presence of wild-type P0 can rescue the
7 effects of the mutation. Correct gene dosage of P0 is important for normal myelination in animal models as
8 well as CMT patients (Fabrizi *et al.* 2006; Maeda *et al.* 2012; Martini *et al.* 1995; Quattrini *et al.* 1999;
9 Speevak and Farrell 2013; Wrabetz *et al.* 2000). The molecular details of the involved mechanisms are
10 currently lacking. Further studies on the D224Y mutation *in vitro* and *in vivo* could help in understanding
11 molecular aspects of both normal and abnormal myelination.

12 Lys236 appears to be a functionally important amino acid in P0ct. In its membrane-bound state, P0ct is likely
13 to have Lys236 close to the lipid headgroups, and altering the charge in this environment might influence
14 folding and the global positioning of P0ct on the membrane. Indeed, a gradual effect in membrane packing
15 was observed in SAXD; the repeat structure loosens, as residue 236 neutralizes (K236del) and turns to
16 negative (K236E). Turbidimetry also indicated a clear effect of charge reversal at residue 236. The Lys236
17 mutants folded to a similar degree as wt-P0ct, which suggests that the role of Lys236 is in packing, rather
18 than folding. This is supported by the slower kinetic parameters for Lys236 mutants in stopped-flow
19 measurements.

20 Similarly to Lys236, Arg227 could harbour a role in membrane packing. In our experiments, R227S is one of
21 the mutants that appeared to induce weaker adhesion than the wild-type protein. The mutation results in a
22 loosened repeat structure without a major impact on protein folding. Arg227 might be involved in
23 electrostatic anchoring of the protein to the lipid headgroups – the R227S mutation likely has low impact on
24 ER stress and UPR, as mutated P0 correctly localizes to the plasma membrane (Lee *et al.* 2010).

25 ***Concluding remarks***

26 To a large extent, the P0ct CMT variants studied here perform similarly to wt-P0ct in controlled simple
27 environments. This might differ *in vivo*, where other components are present and P0 is present in its full-
28 length form. Our characterization is focused on protein-lipid interactions and does not take into account
29 possible protein-protein interactions with MBP, P2, or PMP22, which might be relevant for myelination and
30 disease phenotypes. Nevertheless, we have uncovered critical amino acids in P0 that may contribute to the
31 formation of healthy myelin and be involved in disease mechanisms. These include Arg227, Lys236, and
32 Asp224. Our results shed light on the molecular fundamentals of myelination in the PNS, but more
33 comprehensive studies in biological model systems, as well as on molecular structure and dynamics of
34 native-like myelin, are needed for deciphering the mechanisms of the P0ct mutations causing human
35 neuropathy.

1 Experimental procedures

2 Bioinformatics, mutagenesis, protein expression & purification

3 Secondary structure prediction for P0ct was performed using JPred (Drozdetskiy *et al.* 2015). Mutations
4 were generated in the P0ct pHMGWA expression vector (Busso *et al.* 2005; Raasakka *et al.* 2019b) by PCR
5 using Phusion High-Fidelity DNA polymerase (Thermo Fisher Scientific) with 5'-phosphorylated primers
6 that introduced the desired point mutations. The samples were treated with *Dpn*I (New England Biolabs) to
7 digest template DNA and linear vectors circularized using T4 DNA ligase (New England Biolabs), followed
8 by transformation and plasmid isolation. The presence of mutations and integrity of the constructs was
9 verified using DNA sequencing.

10 Protein expression and purification were carried out in *E. coli* BL21(DE3) as described for wt-P0ct
11 (Raasakka *et al.* 2019b), with the exception of an added amylose-resin affinity step between Ni-NTA and
12 size-exclusion chromatography. The step was introduced to remove any contaminating maltose-binding
13 protein tags from the tobacco etch virus protease-digested recombinant proteins. Size exclusion
14 chromatography was carried out using Superdex S75 16/60 HiLoad and Superdex 75 10/300GL columns
15 (GE Healthcare) with 20 mM HEPES, 150 mM NaCl, pH 7.5 (HBS) as mobile phase, with the exception of
16 D224Y, where a 20 mM Tris-HCl, 300 mM NaCl, pH 8.5 (TBS) solution was used. The monodispersity and
17 R_h of all proteins were checked from filtered 1 mg/ml samples using a Malvern Zetasizer ZS DLS
18 instrument. The D224Y mutant was then dialyzed into HBS. Additionally, all proteins were dialyzed into
19 water prior to SRCD experiments.

20

21 Mass spectrometry

22 The molecular weight and identity of the purified proteins were verified by mass spectrometry. In short, the
23 proteins were subjected to ultra-performance liquid chromatography (UPLC) coupled electrospray ionization
24 (ESI) time-of-flight mass spectrometry in positive ion mode, using a Waters Acquity UPLC-coupled Synapt
25 G2 mass analyzer with a Z-Spray ESI source. This allowed us to determine the undigested masses of each
26 purified P0ct variant. Protein identity and the presence of the desired mutations were confirmed from
27 peptides extracted after in-gel tryptic proteolysis, using a Bruker Ultra fleXtreme matrix-assisted laser
28 desorption/ionization time-of-flight (MALDI-TOF) mass analyzer.

29

30 Small-angle X-ray scattering

31 SAXS data were collected from protein samples at 0.3 – 12.9 mg/ml in HBS and TBS on the EMBL P12
32 beamline, PETRA III (Hamburg, Germany) (Blanchet *et al.* 2015). Monomeric bovine serum albumin (M_r =
33 66.7 kDa; I_0 = 499.0) was used as a molecular weight standard. Data were processed and analyzed using the

1 ATSAS package (Franke *et al.* 2017), and GNOM was used to calculate distance distribution functions
2 (Svergun 1992). See Supplementary Table 2 for further details.

3

4 **Vesicle preparation**

5 DMPC, DMPG, and DOPC were purchased from Larodan Fine Chemicals AB (Malmö, Sweden). DOPS and
6 the deuterated d₅₄-DMPC and d₅₄-DMPG were purchased from Avanti Polar Lipids (Alabaster, Alabama,
7 USA).

8 Lipid stocks were prepared by dissolving dry lipids in chloroform or chloroform:methanol (9:1 v/v) at 10-30
9 mM. Mixtures were prepared from stocks at the desired molar ratios, followed by solvent evaporation under
10 a stream of nitrogen and lyophilizing overnight at -52 °C. The dried lipids were stored at -20 °C or used
11 directly for liposome preparation.

12 Liposomes were prepared by mixing dried lipids with water or HBS at 10-15 mM, followed by inverting at
13 ambient temperature for at least 3 h. Multilamellar vesicles (MLV) were prepared by freeze-thaw cycles in
14 liquid N₂ and a warm water bath and vortexing. The cycle was performed 7 times in total. Large unilamellar
15 vesicles (LUV) were prepared by passing fresh MLVs through a 0.1-μm membrane 11 times at 40 °C. SUVs
16 were prepared by ultrasonication of fresh MLVs using a probe tip sonicator (Sonics & Materials Inc. Vibra-
17 Cell VC-130) until clarified. All lipid preparations were immediately used in experiments.

18

19 **Synchrotron radiation circular dichroism spectroscopy**

20 SRCD spectra were collected from 0.1 – 0.5 mg/ml protein samples in water on the AU-CD beamline at
21 ASTRID2 synchrotron (ISA, Aarhus, Denmark). Samples containing lipids were prepared right before
22 measurement by mixing proteins (P/L ratio 1:200) with SUVs. 100-μm pathlength closed circular cells
23 (Suprasil, Hellma Analytics) were used for the measurements. Spectra were recorded from 170 to 280 nm at
24 30 °C. Baselines were subtracted and CD units converted to $\Delta\epsilon$ (M⁻¹ cm⁻¹) in CDtoolX (Miles and Wallace
25 2018). SDS and TFE were from Sigma-Aldrich and the detergents LDAO, OG, DM, and DPC from
26 Affymetrix.

27 Rapid kinetic SRCD data were collected as described (Raasakka *et al.* 2019a). In short, an SX-20 stopped-
28 flow instrument (Applied Photophysics) mounted on the AU-rSRCD branch line of the AU-AMO beamline
29 at ASTRID2 (ISA, Aarhus, Denmark) was used for data collection at 10 °C. 1-to-1 mixing of a 0.1 mg/ml
30 protein solution and a DMPC:DMPG (1:1) SUV solution (at P/L ratios 1:200) was achieved using a mixer (2
31 ms dead time) before injection into the measurement cell (160 μl total volume, 2-mm pathlength) per shot.
32 The CD signal (mdeg) was monitored at a fixed wavelength of 195 nm for 5 s with a total of 5 – 10 repeat
33 shots per sample, which were averaged into a single curve. Each sample was prepared and measured in

1 duplicate. Water baselines were subtracted from sample data. The data were fitted to different exponential
2 functions using GraphPad Prism 7.

3

4 **Surface plasmon resonance**

5 SPR was performed on a Biacore T200 system (GE Healthcare). According to the manufacturer's
6 instructions, 100-nm LUVs of 1 mM DMPC:DMPG (1:1) were immobilized on an L1 sensor chip (GE
7 Healthcare) in HBS, followed by the injection of protein solutions. Chip regeneration was performed using a
8 2:3 (v:v) mixture of 2-propanol and 50 mM NaOH. The protein concentration was 20 – 2000 nM in HBS,
9 and a single concentration per lipid capture was studied; all samples were prepared and measured in
10 duplicate. In each run, one sample was measured twice to rule out instrumental deviation. The binding
11 response as a function of protein concentration was plotted and fitted to the 4-parameter model,

12
$$R = R_{hi} - \frac{R_{hi} - R_{lo}}{1 + \left(\frac{[P_{oct}]}{A_1}\right)^{A_2}},$$

13 to gain information about association affinity.

14

15 **Differential scanning calorimetry**

16 Proteins were mixed with MLVs in HBS at a protein-to-lipid ratio of 1:100 or 1:250, always containing 350
17 μ M of DMPC:DMPG (1:1) in a final volume of 700 μ l. Lipid samples without proteins were prepared as
18 controls. The samples were degassed for 10 min under vacuum with stirring at 10 °C before measurements.

19 DSC was performed using a MicroCal VP-DSC calorimeter with a cell volume of 527.4 μ l. The reference
20 cell was filled with HBS. Each sample was scanned from 10 to 40 °C and back to 10 °C in 1 °C/min
21 increments. Baselines were subtracted from sample curves and zeroed between 15 & 20 °C to enable
22 straightforward comparison between samples. All samples were prepared and measured twice, with the
23 observed trends being reproducible.

24

25 **Vesicle turbidimetry and X-ray diffraction experiments**

26 For turbidimetric measurements, SUVs of DMPC:DMPG (1:1) were mixed with 0.5 – 10 μ M protein in
27 duplicate and mixed thoroughly. Turbidity was recorded at 450 nm at 30 °C using a Tecan Spark 20M plate
28 reader. Turbidity of protein-free SUVs was subtracted from the protein samples, and statistical analysis was
29 performed using GraphPad Prism 7.

30 SAXD experiments were performed to investigate repetitive structures in the turbid samples. 10 and 20 μ M
31 proteins were mixed with SUVs of 1 – 3 mM DMPC:DMPG (1:1) in HBS at ambient temperature and

1 exposed at 25 °C on the EMBL P12 BioSAXS beamline, DESY (Hamburg, Germany). A HBS buffer
2 reference was subtracted from the data. Lipid samples without added protein did not produce Bragg peaks.
3 The peak positions of momentum transfer, s , in all measured samples were used to calculate mean repeat
4 distances, d , in proteolipid structures, using the equation

5
$$d = \frac{2\pi}{s}, \text{ where } s = \frac{4\pi \sin \theta}{\lambda}.$$

6

7 **Electron microscopy**

8 For negatively stained EM, 740 μM DMPC:DMPG (1:1) SUVs were mixed with proteins using protein-to-
9 lipid ratios of 1:58, 1:100, 1:200, and 1:500 and incubated at 22 °C for 1 h. EM grids were then prepared,
10 stained and imaged as described before (Raasakka *et al.* 2017; Raasakka *et al.* 2019b; Ruskamo *et al.*
11 2017).

12

13 **Neutron reflectometry**

14 Supported lipid bilayers were prepared onto flat (5 Å RMS roughness tolerance) 80 mm × 50 mm × 15 mm
15 Si-crystal blocks (Sil'tronix Silicon Technologies, Archamps, France). Samples were prepared from a
16 chloroform-methanol stock of 1 mg/ml DMPC:DMPG (1:1). Using Langmuir-Blodgett and Langmuir-
17 Schaefer techniques, the two membrane leaflets of the bilayers were deposited sequentially. The surface
18 pressure was kept at a constant 30 mN m⁻¹ during the deposition, as described previously (Barker *et al.* 2016;
19 Hubbard *et al.* 2017; Raasakka *et al.* 2017). All sample blocks were assembled into low-volume
20 measurement flow cells, which were used for *in situ* exchange of solvent and injection of protein samples
21 between reflectometric data collections (Junghans *et al.* 2015).

22 Neutron reflectometric measurements for wt-P0ct were performed as described (Raasakka *et al.* 2017). In
23 short, the D17 neutron reflectometer at the Institut Laue-Langevin (Grenoble, France) was used for data
24 collection at two incident angles (0.8° and 3.2°) (Cubitt and Fragneto 2002). All samples were kept at 30 °C
25 with HBS buffer as the liquid phase, prepared at a final concentration of 95% (v/v) deuterium oxide (D₂O,
26 Sigma-Aldrich) and in H₂O. The deposited bilayers were characterized, before and after the injection of P0ct,
27 at three different solvent contrasts, varying the volume ratio of D₂O and H₂O in to the sample cell: (1) 95%
28 D₂O, (2) Si-matched water (SMW; 38% (v/v) D₂O, 62% (v/v) H₂O), and (3) 100% H₂O. A 0.5 μM P0ct
29 solution was allowed to interact with the membrane for 3 h whilst monitoring reflectivity, until no further
30 changes were observed. Any excess P0ct was washed out from the bulk solution by exchanging 20 cell
31 volumes of solvent slowly through the sample cell. Fitting was performed using Motofit in Igor Pro 7
32 (Nelson 2006).

1 The scattering length densities of the phospholipids were calculated from volume fractions of the lipid
2 components obtained from molecular dynamics simulations (Armen *et al.* 1998), and for the proteins, they
3 were calculated from the sequences and amino acid volumes (Zamyatnin 1972). The P0ct scattering length
4 density, assuming 90% labile hydrogen exchange, was 3.227, 2.324, and $1.722 \times 10^{-6} \text{ \AA}^{-2}$ in 95%, 38%, and
5 0% D₂O, respectively. The errors in the structural parameters for each sublayer were derived from the
6 maximum acceptable variation in the fitted thickness and lipid volume fraction that allowed a fit to be
7 maintained, subject to a constant molecular area constraint required to maintain a planar bilayer geometry.

8 Details of the analysis of supported lipid membrane structure (Vacklin *et al.* 2005) and interaction with
9 soluble proteins (Wacklin *et al.* 2016) using time-of-flight neutron reflection have been described previously.
10 The fraction of P0 in the lipid bilayers was determined by a simultaneous fit to all contrasts, taking into
11 account the change in protein scattering length density with solvent contrast due to H/D exchange of protons
12 on polar residues with the solvent.

13 For mutant comparison to wt-P0ct, NR data for wt-P0ct and D224Y were collected on the INTER neutron
14 reflectometer at ISIS Neutron and Muon Source (Didcot, United Kingdom) at two incident angles (0.7° and
15 2.3°) (Webster *et al.* 2006) covering a total q-range from 0.01 to 0.34 \AA^{-1} , with a resolution of $\Delta q/q=0.03$.
16 The samples were prepared and handled as above.

17
18

1 **Figure legends**

2 **Fig. 1. Overview of P0ct mutations.** (a) The primary sequence of the wt-P0ct construct, corresponding to
3 amino acids 180 – 248 of the human P0 precursor, with an extra N-terminal Gly residue (gray) left behind
4 from affinity tag cleavage. The Cys182 palmitoylation site was mutated into a Leu (green) in all constructs.
5 Putative serine phosphorylation sites are indicated with asterisks. Residues affected by disease mutations are
6 in bold. CMT1B, CMT2I, and DSS point mutations are shown in blue, red, and orange, respectively. The
7 sequence highlighted in yellow corresponds to the neuritogenic segment used in EAN models (de Sèze *et al.*
8 2016). Secondary structure prediction is shown below. (b) SEC traces of wt-P0ct and mutants as determined
9 using a Superdex 75 10/300GL column. Note the slightly earlier retention volume of D224Y, for which the
10 chromatography had to be performed with a different running buffer than for the other variants. The
11 degradation products (red asterisk) present with D224Y could be completely removed using SEC. The final
12 purity of each P0ct variant (4 μ g per lane) as determined using SDS-PAGE is shown as inset. (c) DLS data
13 of P0ct variants display good monodispersity with minimal variation in R_h .

14

15 **Fig. 2. SAXS analysis of P0ct in solution.** (a) SAXS data for P0ct variants. The scattering curves have been
16 offset for clarity. (b) Guinier fits based on SAXS data. Data range is shown within each graph. (c) Distance
17 distributions. (d) Kratky plots. P0ct variant data point coloring is consistent throughout the figure. GNOM
18 fits to the data are shown as black lines in panels (a) and (c).

19

20 **Fig. 3. Folding and lipid binding analysis of P0ct variants.** The folding of wt-P0ct and mutants was
21 studied using SRCD spectropolarimetry in (a) water, (b) 30% TFE, (c) 0.5% SDS, (d) DMPC:DMPG (1:1),
22 and (e) DMPC:DMPG (4:1) at 1:200 P/L ratio in each lipid condition. Additional spectra are presented in
23 Supplementary Fig. S2. (f) SPR measurements were used to determine the affinity of each P0ct variant to
24 immobilized DMPC:DMPG (1:1) vesicles. The colour coding legend in panel (a) for each mutant trace also
25 corresponds to all other traces in subsequent panels.

26

27 **Fig. 4. Analysis of protein-induced lipid structure behavior.** (a) DSC analysis of lipid tail transition
28 behaviour. (b) Turbidimetric analysis of 0.5 mM DMPC:DMPG (1:1) at 5 μ M (gray) and 10 μ M protein
29 concentration (dark red). These proteins concentrations translate to 1:100 and 1:50 P/L ratios, respectively.
30 Error bars represent standard deviation. Statistical analysis was performed using one-way analysis of
31 variance (ANOVA) followed by Dunnett's multiple comparisons test to wt-P0ct turbidity within the same
32 protein concentration series (* : $P < 0.05$; *** : $P < 0.001$). (c) SAXD analysis reveals that D224Y displays a

1 significantly tighter mean repeat distances compared to wt-P0ct, whereas K236E is most loose. The traces
2 have identical colouring to (a).

3

4 **Fig. 5. EM analysis of P0ct mutants.** Negatively stained samples of DMPC:DMPG (1:1) vesicles (a) alone,
5 and with (b) wt-P0ct, (c) T216ER, (d) A221T, (e) D224Y, (f) R227S, (g) K236E, and (h) K236del were
6 imaged at 1:200 P/L ratio. D224Y forms multilayered lipid structures that are absent for wt-P0ct.

7

8 **Fig. 6. SRCD stopped-flow kinetics of protein-induced initial lipid turbidification.** (a) The SRCD signal
9 evolution was monitored using rapid kinetics at 195 nm for 5 sec. wt-P0ct and mutants were mixed with
10 DMPC:DMPG (1:1) lipids at 1:200 P/L ratio in the presence of 150 mM NaF. Fits (dashed lines) are plotted
11 over the measurement points. Error bars represent standard deviation. See Table 4 for fitting results. (b)
12 Graphical comparison of the obtained k_1 values.

13

14 **Fig. 7. NR data and fitting.** (a) NR data of a supported DMPC:DMPG (1:1) bilayer before (open markers)
15 and after incubation with wt-P0ct (closed markers). The used solvent contrasts were 95% D₂O (red), Si-
16 matched water (SMW, 38% D₂O; green) and 100% H₂O (blue). Fits are shown as dashed and solid lines for
17 the bilayer before and after addition of wt-P0ct, respectively. (b) Scattering length density (ρ) profiles
18 obtained from the fitting. The error bars denote standard deviation. (c) Model for the P0ct-bound membrane.
19 The protein-free membrane is shown in light gray on the background.

20

21

1 **Tables**

2

3 **Table 1. Recombinant protein characterization.**

Variant*	Condition	pI**	Purification		Molecular weight determination		Peptide fingerprinting	
			Yield***	Solubility	Measured	Theoretical***	Difference	Mutation confirmed
wt-P0ct	-	11.11	2.1 ± 0.4	++	7989.0	7990.35	-1.35	-
T216ER	CMT1	11.08	4.2 ± 0.4	+++	8173.0	8174.54	-1.54	yes
A221T	DSS	11.11	5.0 ± 0.7	+++	8018.0	8020.37	-2.37	yes
D224Y	CMT1	11.12	0.8 ± 0.3	+	8037.0	8038.43	-1.43	yes
R227S	CMT1	10.89	6.1 ± 2.0	+++	7919.0	7921.24	-2.24	yes
K236E	CMT2	10.85	5.1 ± 1.8	+++	7989.0	7991.29	-2.29	yes
K236del	CMT1	11.09	5.2 ± 1.0	+++	7860.0	7862.17	-2.17	yes

4 * All proteins, including wt-P0ct, contain the C182L mutation.

5 **Values determined from protein sequences using ProtParam

6 ***Expressed as mg protein obtained on average per liter culture. See Supplementary Fig. 1 for graphical
7 representation.

8

9 **Table 2. SPR fitting parameters.**

Variant	R _{hi}	R _{lo}	A ₁	A ₂	R ²
wt-P0ct	2975 ± 79	-69.10 ± 61.54	363.2 ± 15.1	3.237 ± 0.411	0.9858
T216ER	3123 ± 86	-44.63 ± 64.19	375.1 ± 15.6	3.173 ± 0.409	0.9854
A221T	3061 ± 82	-44.81 ± 62.30	357.0 ± 15.5	2.973 ± 0.363	0.9863
D224Y	3811 ± 81	11.30 ± 66.26	385.2 ± 11.3	4.416 ± 0.540	0.9886
R227S	2798 ± 78	-39.52 ± 55.20	384.9 ± 16.0	2.936 ± 0.361	0.9864
K236E	2671 ± 92	-49.48 ± 60.00	380.8 ± 20.0	2.526 ± 0.340	0.9831
K236del	2880 ± 79	-33.85 ± 58.90	356.1 ± 16.0	2.852 ± 0.347	0.9862

10

11

12

13 **Table 3. Kinetic constants for protein-induced vesicle turbidity.** The kinetic constants were obtained by
14 fitting the data to a two-phase exponential decay function. All errors represent standard deviation.

15

Variant	k ₁ (s ⁻¹)	k ₂ (s ⁻¹)	k ₁ /k ₂	R ²
wt-P0ct	20.14 ± 0.25	1.12 ± 0.01	17.96 ± 0.22	0.9934
T216ER	19.54 ± 0.28	1.18 ± 0.02	16.63 ± 0.25	0.9908
A221T	19.15 ± 0.21	1.14 ± 0.01	16.76 ± 0.20	0.9943
D224Y	22.11 ± 0.28	1.19 ± 0.02	18.53 ± 0.25	0.9923
R227S	19.35 ± 0.27	1.08 ± 0.02	17.95 ± 0.26	0.9916
K236E	14.98 ± 0.12	1.02 ± 0.01	14.64 ± 0.13	0.9969
K236del	14.25 ± 0.12	1.05 ± 0.01	13.54 ± 0.13	0.9967

1
2

3 **Table 4. NR parameters.**

		Bilayer alone	Bilayer with 0.5 μM wt-P0ct
Substrate	Oxide thickness (Å)	10.6	11
	Oxide solvation (%)	0	0
	Oxide roughness (Å)	4	4
	Hydration layer between oxide and bilayer (Å)	4.6	12
	Hydration layer roughness (Å)	3	6
Bilayer	Bilayer area-per-molecule (Å ² /molecule)	60	70
	Inner headgroups thickness (Å)	8.3	8
	Inner headgroups roughness (Å)	3.6	8.1
	Inner headgroups solvation (%)	35	45
	Acyl tails thickness (Å)	28.8	32
	Acyl tails roughness (Å)	3.8	13.3
	Acyl tails hydration (%)	0	17
	Outer headgroups thickness (Å)	8.8	8
	Outer headgroups roughness (Å)	4.9	9.5
	Outer headgroups solvation (%)	35	53.5
wt-P0ct	Protein in inner headgroups (%)		0
	Protein in acyl tails (%)		10
	Protein in outer headgroups (%)		20
	Protein layer thickness (Å)		7
	Protein layer roughness (Å)		15
	Protein layer solvation (%)		86

4
5
6

1 References

2 Armen R.S., Uitto O.D. and Feller S.E. (1998) Phospholipid component volumes: determination
3 and application to bilayer structure calculations. *Biophys J* 75, 734-744.

4 Bai Y., Patzko A. and Shy M.E. (2013) Unfolded protein response, treatment and CMT1B. *Rare*
5 *Dis* 1, e24049.

6 Bai Y., Wu X., Brennan K.M., Wang D.S., D'Antonio M., Moran J., Svaren J. and Shy M.E. (2018)
7 Myelin protein zero mutations and the unfolded protein response in Charcot Marie Tooth
8 disease type 1B. *Ann Clin Transl Neurol* 5, 445-455.

9 Barker R.D., McKinley L.E. and Titmuss S. (2016) Neutron Reflectivity as a Tool for Physics-
10 Based Studies of Model Bacterial Membranes. *Adv Exp Med Biol* 915, 261-282.

11 Blanchet C.E., Spilotros A., Schwemmer F., Graewert M.A., Kikhney A., Jeffries C.M., Franke D.,
12 Mark D., Zengerle R., Cipriani F., Fiedler S., Roessle M. and Svergun D.I. (2015) Versatile
13 sample environments and automation for biological solution X-ray scattering experiments at
14 the P12 beamline (PETRA III, DESY). *J Appl Crystallogr* 48, 431-443.

15 Busso D., Delagoutte-Busso B. and Moras D. (2005) Construction of a set Gateway-based
16 destination vectors for high-throughput cloning and expression screening in *Escherichia coli*.
17 *Anal Biochem* 343, 313-321.

18 Choi B.O., Lee M.S., Shin S.H., Hwang J.H., Choi K.G., Kim W.K., Sunwoo I.N., Kim N.K. and
19 Chung K.W. (2004) Mutational analysis of PMP22, MPZ, GJB1, EGR2 and NEFL in Korean
20 Charcot-Marie-Tooth neuropathy patients. *Hum Mutat* 24, 185-186.

21 Cubitt R. and Fragneto G. (2002) D17: the new reflectometer at the ILL. *Applied Physics A* 74,
22 s329-s331.

23 de Sèze J., Kremer L., Alves do Rego C., Taleb O., Lam D., Beiano W., Mensah-Nyagan G.,
24 Trifilieff E. and Brun S. (2016) Chronic inflammatory demyelinating polyradiculoneuropathy:
25 A new animal model for new therapeutic targets. *Rev Neurol (Paris)* 172, 767-769.

26 Drozdetskiy A., Cole C., Procter J. and Barton G.J. (2015) JPred4: a protein secondary structure
27 prediction server. *Nucleic Acids Res* 43, W389-94.

28 Eichberg J. (2002) Myelin P0: new knowledge and new roles. *Neurochem Res* 27, 1331-1340.

29 Fabrizi G.M., Pellegrini M., Angiari C., Cavallaro T., Morini A., Taioli F., Cabrini I., Orrico D. and
30 Rizzuto N. (2006) Gene dosage sensitivity of a novel mutation in the intracellular domain of
31 P0 associated with Charcot-Marie-Tooth disease type 1B. *Neuromuscul Disord* 16, 183-187.

32 Filbin M.T., Walsh F.S., Trapp B.D., Pizzey J.A. and Tennekoon G.I. (1990) Role of myelin P0
33 protein as a homophilic adhesion molecule. *Nature* 344, 871-872.

34 Franke D., Petoukhov M.V., Konarev P.V., Panjkovich A., Tuukkanen A., Mertens H.D.T.,
35 Kikhney A.G., Hajizadeh N.R., Franklin J.M., Jeffries C.M. and Svergun D.I. (2017) ATSAS
36 2.8: a comprehensive data analysis suite for small-angle scattering from macromolecular
37 solutions. *J Appl Crystallogr* 50, 1212-1225.

38 Greenfield S., Brostoff S., Eylar E.H. and Morell P. (1973) Protein composition of myelin of the
39 peripheral nervous system. *J Neurochem* 20, 1207-1216.

40 Hartline D.K. (2008) What is myelin? *Neuron Glia Biol* 4, 153-163.

41 Hubbard A.T., Barker R., Rehal R., Vandera K.A., Harvey R.D. and Coates A.R. (2017)
42 Mechanism of Action of a Membrane-Active Quinoline-Based Antimicrobial on Natural and
43 Model Bacterial Membranes. *Biochemistry* 56, 1163-1174.

44 Junghans A., Watkins E.B., Barker R.D., Singh S., Waltman M.J., Smith H.L., Pocivavsek L. and
45 Majewski J. (2015) Analysis of biosurfaces by neutron reflectometry: from simple to complex
46 interfaces. *Biointerphases* 10, 019014.

47 Kidd G.J., Yadav V.K., Huang P., Brand S.L., Low S.H., Weimbs T. and Trapp B.D. (2006) A dual
48 tyrosine-leucine motif mediates myelin protein P0 targeting in MDCK cells. *Glia* 54, 135-145.

49 Lee M., Brennan A., Blanchard A., Zoidl G., Dong Z., Tabernero A., Zoidl C., Dent M.A., Jessen

1 K.R. and Mirsky R. (1997) P0 is constitutively expressed in the rat neural crest and embryonic
2 nerves and is negatively and positively regulated by axons to generate non-myelin-forming
3 and myelin-forming Schwann cells, respectively. *Mol Cell Neurosci* 8, 336-350.

4 Lee Y.C., Lin K.P., Chang M.H., Liao Y.C., Tsai C.P., Liao K.K. and Soong B.W. (2010) Cellular
5 characterization of MPZ mutations presenting with diverse clinical phenotypes. *J Neurol* 257,
6 1661-1668.

7 Lemke G. and Axel R. (1985) Isolation and sequence of a cDNA encoding the major structural
8 protein of peripheral myelin. *Cell* 40, 501-508.

9 Luo X., Sharma D., Inouye H., Lee D., Avila R.L., Salmona M. and Kirschner D.A. (2007)
10 Cytoplasmic domain of human myelin protein zero likely folded as beta-structure in compact
11 myelin. *Biophys J* 92, 1585-1597.

12 Maeda M.H., Mitsui J., Soong B.W., Takahashi Y., Ishiura H., Hayashi S., Shirota Y., Ichikawa Y.,
13 Matsumoto H., Arai M., Okamoto T., Miyama S., Shimizu J., Inazawa J., Goto J. and Tsuji S.
14 (2012) Increased gene dosage of myelin protein zero causes Charcot-Marie-Tooth disease.
15 *Ann Neurol* 71, 84-92.

16 Mandich P., Fossa P., Capponi S., Geroldi A., Acquaviva M., Gulli R., Ciotti P., Manganelli F.,
17 Grandis M. and Bellone E. (2009) Clinical features and molecular modelling of novel MPZ
18 mutations in demyelinating and axonal neuropathies. *Eur J Hum Genet* 17, 1129-1134.

19 Martini R., Zielasek J., Toyka K.V., Giese K.P. and Schachner M. (1995) Protein zero (P0)-
20 deficient mice show myelin degeneration in peripheral nerves characteristic of inherited
21 human neuropathies. *Nat Genet* 11, 281-286.

22 Miles A.J. and Wallace B.A. (2018) CDtoolX, a downloadable software package for processing and
23 analyses of circular dichroism spectroscopic data. *Protein Sci* 27, 1717-1722.

24 Miltenberger-Miltenyi G., Schwarzbraun T., Löscher W.N., Wanschitz J., Windpassinger C., Duba
25 H.C., Seidl R., Albrecht G., Weirich-Schwaiger H., Zoller H., Utermann G., Auer-Grumbach
26 M. and Janecke A.R. (2009) Identification and in silico analysis of 14 novel GJB1, MPZ and
27 PMP22 gene mutations. *Eur J Hum Genet* 17, 1154-1159.

28 Nelson A. (2006) Co-refinement of multiple-contrast neutron/X-ray reflectivity data using
29 MOTOFIT. *J Appl Crystallogr* 39, 273-276.

30 Patzig J., Jahn O., Tenzer S., Wichert S.P., de Monasterio-Schrader P., Rosfa S., Kuharev J., Yan
31 K., Bormuth I., Bremer J., Aguzzi A., Orfaniotou F., Hesse D., Schwab M.H., Möbius W.,
32 Nave K.A. and Werner H.B. (2011) Quantitative and integrative proteome analysis of
33 peripheral nerve myelin identifies novel myelin proteins and candidate neuropathy loci. *J*
34 *Neurosci* 31, 16369-16386.

35 Planté-Bordeneuve V., Parman Y., Guiochon-Mantel A., Alj Y., Deymeer F., Serdaroglu P.,
36 Eraksoy M. and Said G. (2001) The range of chronic demyelinating neuropathy of infancy: a
37 clinico-pathological and genetic study of 15 unrelated cases. *J Neurol* 248, 795-803.

38 Quattrini A., Feltri M.L., Previtali S., Fasolini M., Messing A. and Wrabetz L. (1999) Peripheral
39 nerve dysmyelination due to P0 glycoprotein overexpression is dose-dependent. *Ann N Y*
40 *Acad Sci* 883, 294-301.

41 Raasakka A., Jones N.C., Hoffmann S.V. and Kursula P. (2019a) Ionic strength and calcium
42 regulate the membrane interactions of myelin basic protein and the cytoplasmic domain of
43 myelin protein zero. *bioRxiv* 529586.

44 Raasakka A., Ruskamo S., Kowal J., Barker R., Baumann A., Martel A., Tuusa J., Myllykoski M.,
45 Bürck J., Ulrich A.S., Stahlberg H. and Kursula P. (2017) Membrane Association Landscape
46 of Myelin Basic Protein Portrays Formation of the Myelin Major Dense Line. *Sci Rep* 7,
47 4974.

48 Raasakka A., Ruskamo S., Kowal J., Han H., Baumann A., Myllykoski M., Fasano A., Rossano R.,
49 Riccio P., Bürck J., Ulrich A.S., Stahlberg H., Kursula P. and (2019b) Molecular structure and
50 function of myelin protein P0 in membrane stacking. *Sci Rep* 9, 642.

1 Ruskamo S., Nieminen T., Kristiansen C.K., Vatne G.H., Baumann A., Hallin E.I., Raasakka A.,
2 Joensuu P., Bergmann U., Vattulainen I. and Kursula P. (2017) Molecular mechanisms of
3 Charcot-Marie-Tooth neuropathy linked to mutations in human myelin protein P2. *Sci Rep* 7,
4 6510.

5 Ruskamo S., Yadav R.P., Sharma S., Lehtimäki M., Laulumaa S., Aggarwal S., Simons M., Bürck
6 J., Ulrich A.S., Juffer A.H., Kursula I. and Kursula P. (2014) Atomic resolution view into the
7 structure-function relationships of the human myelin peripheral membrane protein P2. *Acta
8 Crystallogr D Biol Crystallogr* 70, 165-176.

9 Schneider-Gold C., Kötting J., Epplen J.T., Gold R. and Gerding W.M. (2010) Unusual Charcot-
10 Marie-Tooth phenotype due to a mutation within the intracellular domain of myelin protein
11 zero. *Muscle Nerve* 41, 550-554.

12 Sedzik J., Blaurock A.E. and Hoechli M. (1985) Reconstituted P2/myelin-lipid multilayers. *J
13 Neurochem* 45, 844-852.

14 Shapiro L., Doyle J.P., Hensley P., Colman D.R. and Hendrickson W.A. (1996) Crystal structure of
15 the extracellular domain from P0, the major structural protein of peripheral nerve myelin.
16 *Neuron* 17, 435-449.

17 Shy M.E., Jáni A., Krajewski K., Grandis M., Lewis R.A., Li J., Shy R.R., Balsamo J., Lilien J.,
18 Garbern J.Y. and Kamholz J. (2004) Phenotypic clustering in MPZ mutations. *Brain* 127, 371-
19 384.

20 Speevak M.D. and Farrell S.A. (2013) Charcot-Marie-Tooth 1B caused by expansion of a familial
21 myelin protein zero (MPZ) gene duplication. *Eur J Med Genet* 56, 566-569.

22 Stassart R.M., Möbius W., Nave K.A. and Edgar J.M. (2018) The Axon-Myelin Unit in
23 Development and Degenerative Disease. *Front Neurosci* 12, 467.

24 Street V.A., Meekins G., Lipe H.P., Seltzer W.K., Carter G.T., Kraft G.H. and Bird T.D. (2002)
25 Charcot-Marie-Tooth neuropathy: clinical phenotypes of four novel mutations in the MPZ and
26 Cx 32 genes. *Neuromuscul Disord* 12, 643-650.

27 Su Y., Brooks D.G., Li L., Lepercq J., Trofatter J.A., Ravetch J.V. and Lebo R.V. (1993) Myelin
28 protein zero gene mutated in Charcot-Marie-tooth type 1B patients. *Proc Natl Acad Sci U S A*
29 90, 10856-10860.

30 Suresh S., Wang C., Nanekar R., Kursula P. and Edwardson J.M. (2010) Myelin basic protein and
31 myelin protein 2 act synergistically to cause stacking of lipid bilayers. *Biochemistry* 49, 3456-
32 3463.

33 Svergun D.I. (1992) Determination of the regularization parameter in indirect-transform methods
34 using perceptual criteria. *J Appl Cryst* 25, 495-503.

35 Vacklin H.P., Tiberg F., Fragneto G. and Thomas R.K. (2005) Composition of supported model
36 membranes determined by neutron reflection. *Langmuir* 21, 2827-2837.

37 Vassall K.A., Bamm V.V. and Harauz G. (2015) MyelStones: the executive roles of myelin basic
38 protein in myelin assembly and destabilization in multiple sclerosis. *Biochem J* 472, 17-32.

39 Wacklin H.P., Bremec B.B., Moulin M., Rojko N., Haertlein M., Forsyth T., Anderluh G. and
40 Norton R.S. (2016) Neutron reflection study of the interaction of the eukaryotic pore-forming
41 actinoporin equinatoxin II with lipid membranes reveals intermediate states in pore formation.
42 *Biochim Biophys Acta* 1858, 640-652.

43 Wang C., Neugebauer U., Bürck J., Myllykoski M., Baumgärtel P., Popp J. and Kursula P. (2011)
44 Charge isomers of myelin basic protein: structure and interactions with membranes,
45 nucleotide analogues, and calmodulin. *PLoS One* 6, e19915.

46 Webster J., Holt S. and Dalglish R. (2006) INTER the chemical interfaces reflectometer on target
47 station 2 at ISIS. *Physica B: Condensed Matter* 385, 1164-1166.

48 Wong M.H. and Filbin M.T. (1994) The cytoplasmic domain of the myelin P0 protein influences
49 the adhesive interactions of its extracellular domain. *J Cell Biol* 126, 1089-1097.

50 Wrabetz L., D'Antonio M., Pennuto M., Dati G., Tinelli E., Fratta P., Previtali S., Imperiale D.,

1 Zielasek J., Toyka K., Avila R.L., Kirschner D.A., Messing A., Feltri M.L. and Quattrini A.
2 (2006) Different intracellular pathomechanisms produce diverse Myelin Protein Zero
3 neuropathies in transgenic mice. *J Neurosci* 26, 2358-2368.

4 Wrabetz L., Feltri M.L., Quattrini A., Imperiale D., Previtali S., D'Antonio M., Martini R., Yin X.,
5 Trapp B.D., Zhou L., Chiu S.Y. and Messing A. (2000) P(0) glycoprotein overexpression
6 causes congenital hypomyelination of peripheral nerves. *J Cell Biol* 148, 1021-1034.

7 Xu W., Shy M., Kamholz J., Elferink L., Xu G., Lilien J. and Balsamo J. (2001) Mutations in the
8 cytoplasmic domain of P0 reveal a role for PKC-mediated phosphorylation in adhesion and
9 myelination. *J Cell Biol* 155, 439-446.

10 Zamyatnin A.A. (1972) Protein volume in solution. *Prog Biophys Mol Biol* 24, 107-123.

11 Zenker J., Stettner M., Ruskamo S., Domènech-Estévez E., Baloui H., Médard J.J., Verheijen M.H.,
12 Brouwers J.F., Kursula P., Kieseier B.C. and Chrast R. (2014) A role of peripheral myelin
13 protein 2 in lipid homeostasis of myelinating Schwann cells. *Glia* 62, 1502-1512.

14

15

1 **Acknowledgements**

2 This work was financially supported by the Academy of Finland (Finland), the Jane and Aatos Erkko
3 Foundation (Finland), and the Norwegian Research Council (SYNKNØYT program). This work has been
4 supported by iNEXT, grant number 653706, funded by the Horizon 2020 programme of the European
5 Commission. The research leading to this result has been supported by the project CALIPSOplus under the
6 Grant Agreement 730872 from the EU Framework Programme for Research and Innovation HORIZON
7 2020. We gratefully acknowledge the synchrotron radiation facilities and the beamline support at ASTRID2
8 and EMBL/DESY, as well as the ILL (Proposal No. 8-02-745) and STFC/ISIS (Proposal No. 1620422;
9 doi:10.5286/ISIS.E.95673822). We express our gratitude towards the Biocenter Oulu Proteomics and Protein
10 Analysis Core Facility for providing access to mass spectrometric instrumentation, as well as the Biophysics,
11 Structural Biology, and Screening (BiSS) facilities at the University of Bergen. Finally, we thank Anushik
12 Safaryan for practical help with liposome preparation.

13

14 **Author contributions**

15 Original text and figures: A.R., P.K.
16 Prepared mutant constructs: A.R., C.K.K., G.H.V., E.I.H.
17 Protein expression and purification: A.R., O.C.K.
18 Prepared samples and performed experiments: A.R., S.R., R.B., M.W.A.S., U.B.
19 Processed and analyzed data: A.R., R.B., U.B., H.W., N.J., S.V.H., P.K.
20 Study design: A.R., S.R., P.K.
21 Review & editing: A.R., S.R., R.B., H.W., N.J., S.V.H., P.K.
22 Supervision: P.K.

23

24 **Competing financial interests**

25 The authors declare no competing financial interests.

26

27 **Data availability**

28 The datasets generated and analyzed during the current study are available from the corresponding author on
29 reasonable request.

1 **Supplementary information**

2

3 **Supplementary Fig. S1. Protein yield.** The purified protein amount from *E. coli* expression, shown as mg
4 of protein obtained per 1 l of culture.

5

6 **Supplementary Fig. S2. The folding of P0ct variants in TFE, detergents, and poorly binding
7 membrane compositions.** The folding of wt-P0ct and mutants was studied using SRCD spectropolarimetry
8 in (a) 10% TFE, (b) 50% TFE, (c) 70% TFE, (d) 0.1% DPC, (e) 1% LDAO, (f) 1% OG, (g) DMPC, and (h)
9 9:1 DMPC:DMPG. The colour coding legend in panel (a) for each mutant trace also corresponds to all other
10 traces in subsequent panels.

11

12 **Supplementary Fig. S3. P0ct variant-induced turbidimetry and diffraction.** (a) Turbidimetric analysis of
13 0.5 mM DMPC:DMPG (1:1) vesicles in the presence of 0 – 10 μ M wt-P0ct and mutants. BSA was included
14 as negative control. Error bars represent standard deviation. (b) Examples of Bragg peaks from the P0ct
15 samples mixed with DMPC:DMPG (1:1) vesicles.

16

17 **Supplementary Fig. S4. EM analysis of P0ct D224Y.** Negatively stained samples of DMPC:DMPG (1:1)
18 vesicles mixed with P0ct D224Y at (a) 1:100, (b) 1:200, and (c) 1:500 P/L ratios all display multilayered
19 lipid structures.

20

21 **Supplementary Fig. S5. NR data of wt-P0ct and D224Y.** NR data for DMPC:DMPG (1:1)-bound wt-P0ct
22 and D224Y. The data have been offset for clarity. Solvent contrasts are indicated for each trace on their right
23 hand side. The D224Y H_2O data is incomplete as reflectivity was collected at only one measurement angle
24 (0.7°). The error bars denote standard deviation.

25

26

1 **Supplementary Table 1.** DLS parameters.

Protein variant	wt-P0ct	T216ER	A221T	D224Y	R227S	K236E	K236del
Sample buffer*	HBS	HBS	HBS	TBS	HBS	HBS	HBS
R_h (nm)	2.96	2.87	2.72	2.26	2.93	2.88	2.80

2 *HBS, 20 mM HEPES, 150 mM NaCl, pH 7.5; TBS, 20 mM Tris-HCl, 300 mM NaCl, pH 8.5.

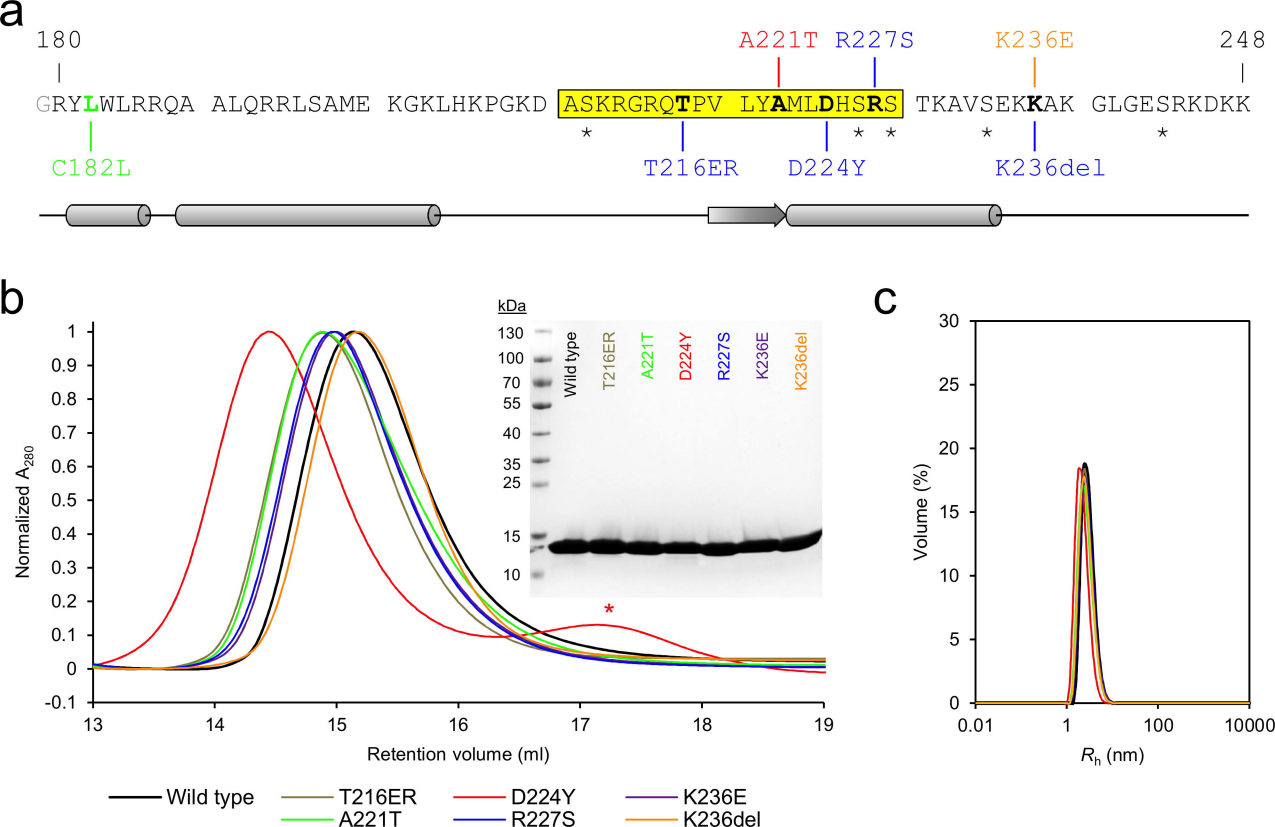
3

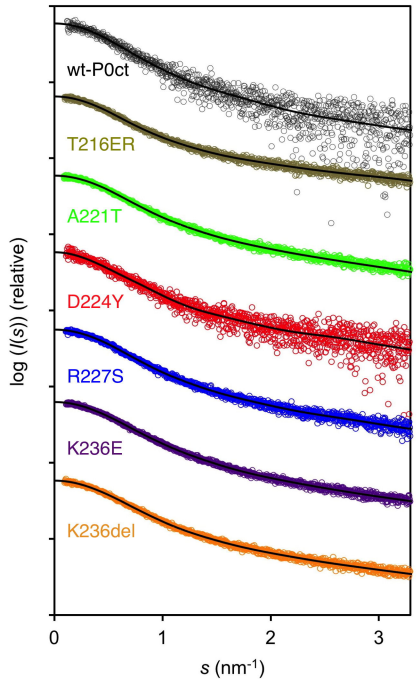
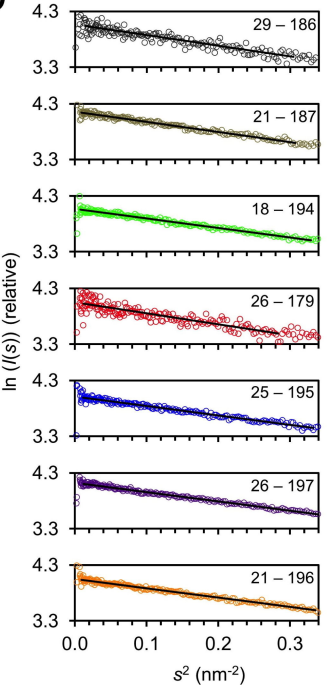
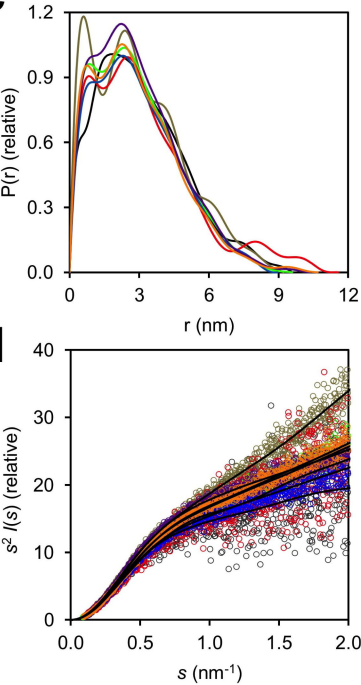
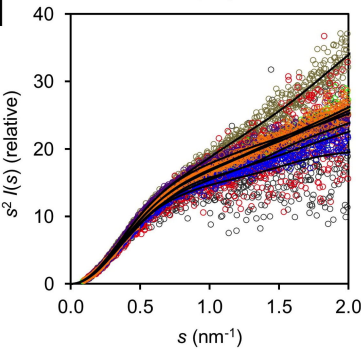
4 **Supplementary Table 2.** SAXS parameters.

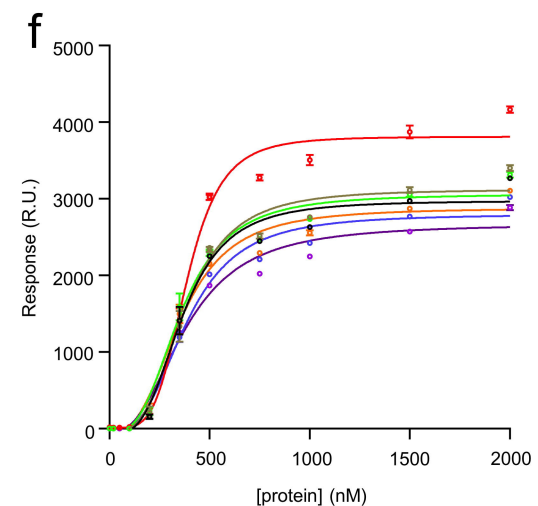
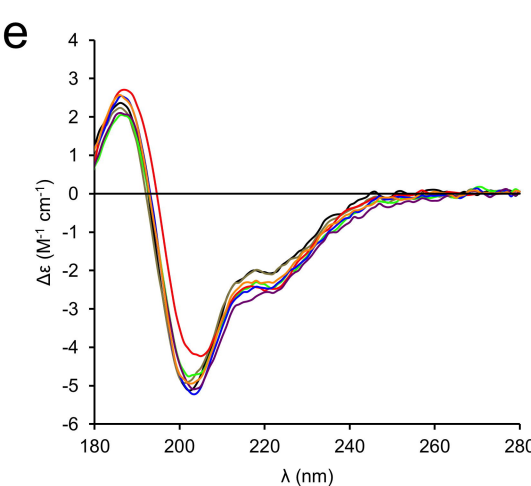
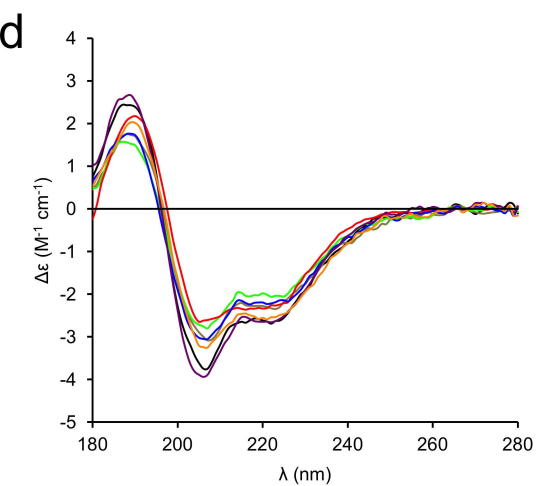
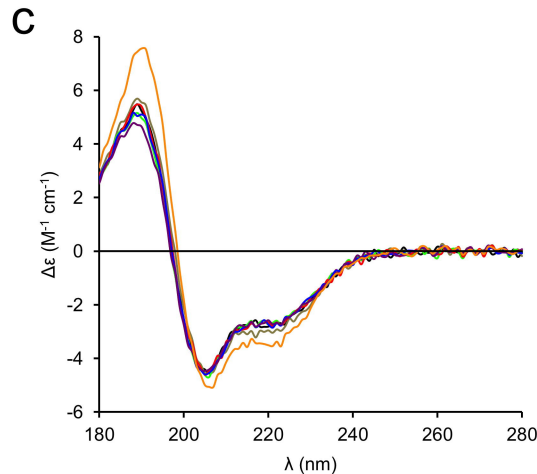
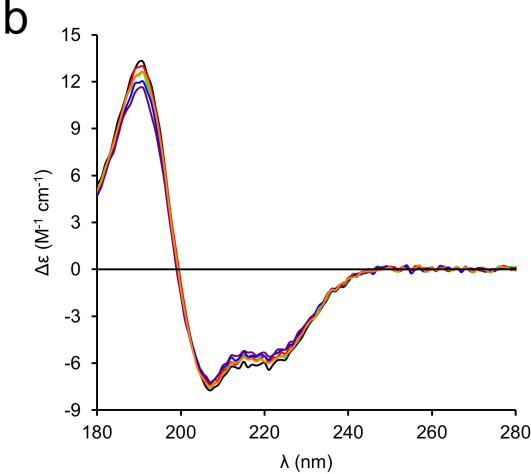
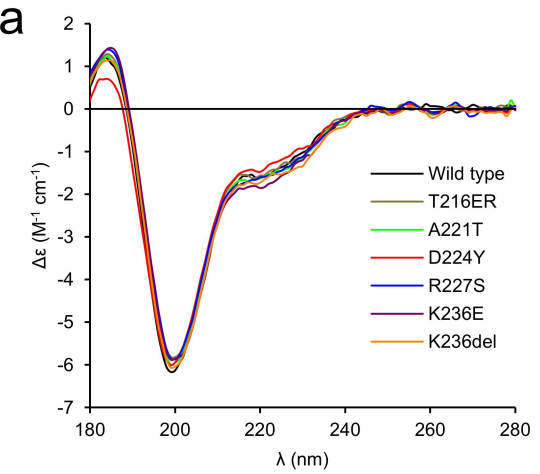
Data collection parameters							
Instrument	P12, PETRAIII, DESY						
Wavelength (nm)	0.124						
Angular range (nm ⁻¹)	0.0403 - 7.3195						
Exposure time (s)	0.045						
Measurement temperature (°C)	10						
Protein variant	wt-P0ct	T216ER	A221T	D224Y	R227S	K236E	K236del
Concentration range (mg ml ⁻¹)	0.3 - 1.2	1.0 - 3.8	2.0 - 8.0	0.5 - 2.1	1.7 - 6.8	3.5 - 12.9	2.3 - 9.3
Sample buffer*	HBS	HBS	HBS	TBS	HBS	HBS	HBS
Structural parameters							
I_0 (relative) [from p(r)]	58.90	64.72	59.06	58.27	56.14	62.73	58.17
R_g (nm) [from p(r)]	2.57	2.50	2.40	2.73	2.42	2.41	2.41
I_0 (relative) [from Guinier]	58.25	63.87	58.35	57.38	55.21	61.61	57.30
R_g (nm) [from Guinier]	2.39	2.33	2.26	2.43	2.25	2.23	2.23
D_{\max} (nm) [from GNOM]	9.59	9.21	9.59	11.57	8.96	10.34	10.69
Molecular mass determination							
Molecular mass M_r (kDa) [from I_0 using p(r)]	7.87	8.65	7.89	7.79	7.50	8.38	7.78
Molecular mass M_r (kDa) [from I_0 using Guinier]	7.79	8.54	7.80	7.67	7.38	8.24	7.66
Theoretical M_r from sequence (kDa)	7.99	8.17	8.02	8.04	7.92	7.99	7.86
Software							
Primary data reduction & processing	PRIMUS						

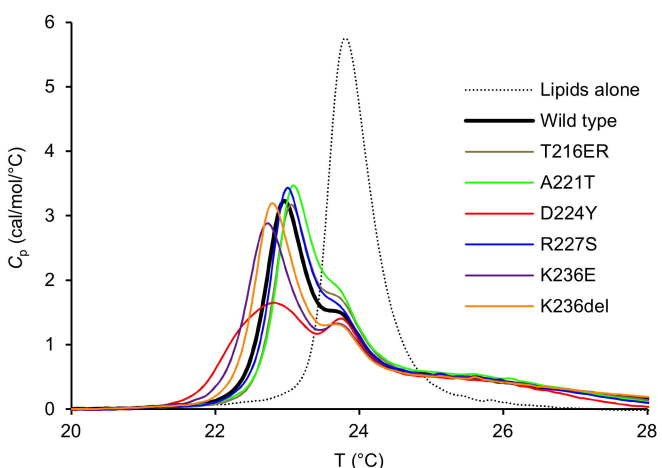
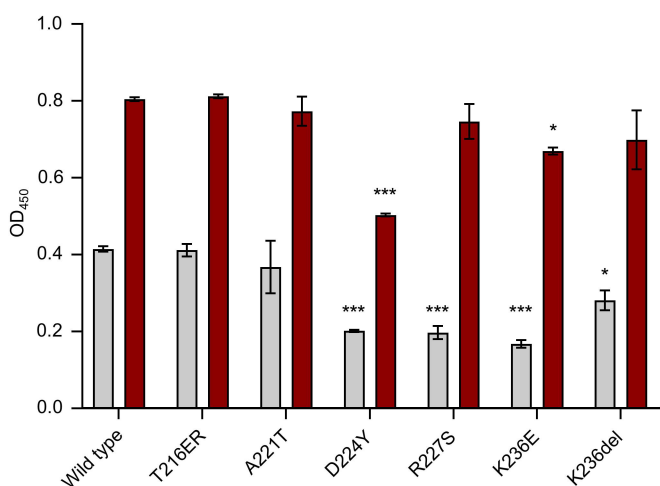
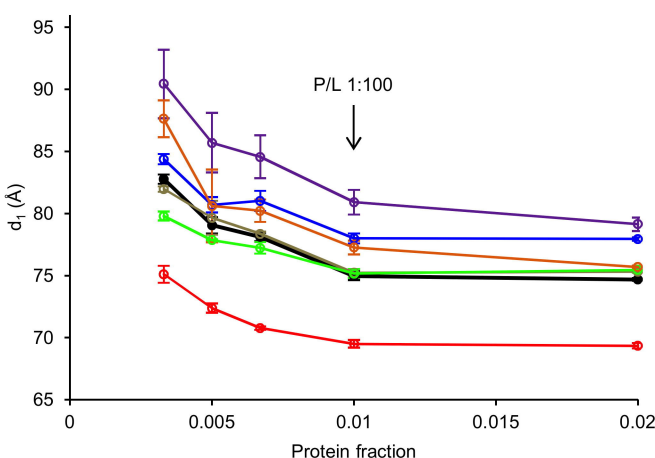
5 *HBS, 20 mM HEPES, 150 mM NaCl, pH 7.5; TBS, 20 mM Tris-HCl, 300 mM NaCl, pH 8.5.

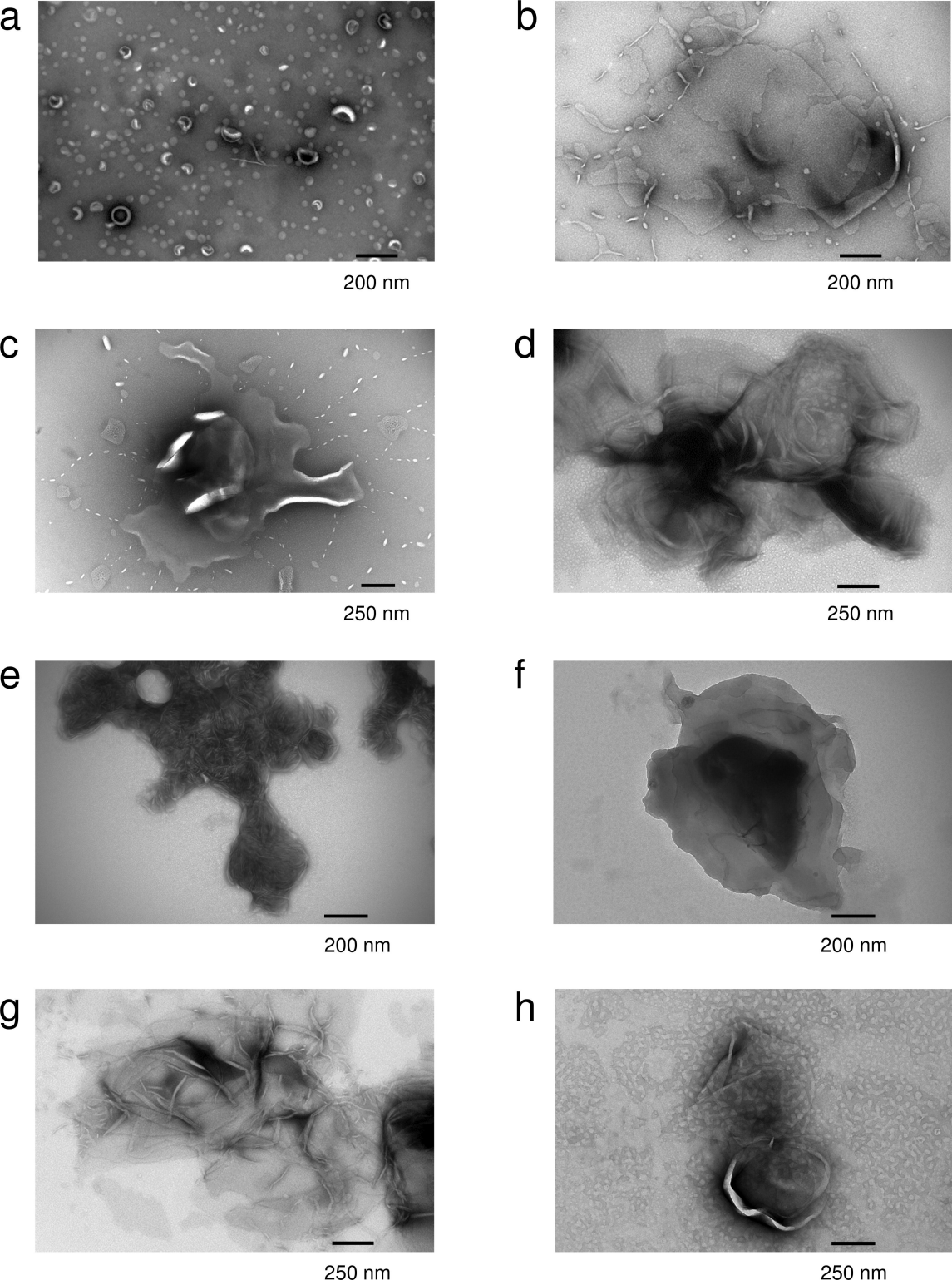
6

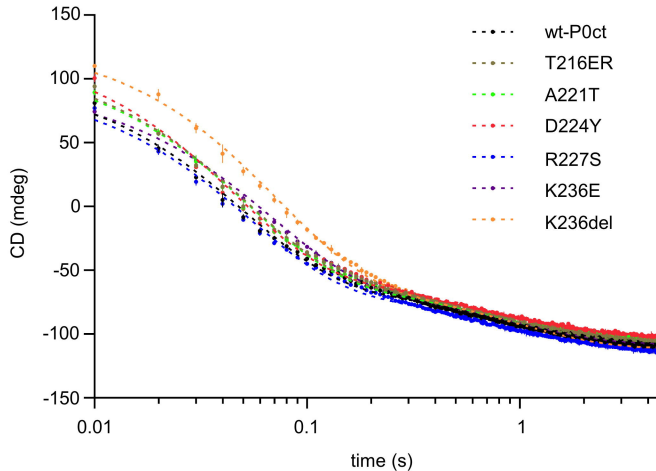


a**b****c****d**



a**b****c**



a**b**